Tribology International 204 (2025) 110439

Contents lists available at ScienceDirect

Tribology International

journal homepage: www.elsevier.com/locate/triboint

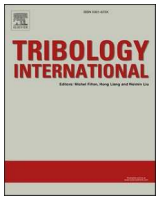

Accurate measurement of particle velocity using a double disc anemometer in erosive wear experiments

William Cashmore [a], Alexander Blanchard [b], Getu Hailu [a,*]

[a] University of Alaska Anchorage, USA
[b] NASA Marshall Space Flight Center (MSFC), USA

ARTICLE INFO

Keywords:
Abrasive particle velocity
Double disc anemometer
Laser doppler velocimetry
Particle velocity uncertainty
Solid particle erosion

ABSTRACT

Accurately characterizing abrasive particle velocity ejected from a nozzle in a pressurized airflow is crucial for solid particle erosion quantification, abrasive jet micromachining, and abrasive slurry micro-jet experiments. A double-disc anemometer (DDA) is an economical particle velocity measurement apparatus which is cost effective to implement. The DDA method determines particle velocity using the time it takes for particles to travel a known distance between two rotating discs mounted on the same shaft. Since 1975, the DDA has been used to measure solid particle velocities in gas-particulate flow streams. Particle velocity measurement using a DDA is an intricate process, which the experimental procedure lacks published standardization outlining, operation procedures, comprehensive error analysis, and post-processing advice, all required to report accurate and reliable results. This paper presents a new and improved DDA design, automated post-processing procedures, and experimental validation characterizing the flow development of 66 μm glass bead abrasive blasted with a maximum mean particle velocity of 95.3m/s. State-of-the-art laser Doppler velocimetry equipment (LDV) was used to validate the DDA results with an agreement of -2.8 % on average. Further, this paper investigates the disc separation distance and shaft angular velocity, discussing configuration recommendations for reliable measurements, with an optimal reported uncertainty of $\pm$ 3.2 %. Finally, a novel scarring analysis method was conducted to identify the intricacies of how the instrument's geometries affect the velocity calculation.

1. Introduction

1.1. Solid particle erosion

Generally, the wear process in manufacturing is the term used to describe the slow degradation of machine parts brought on by friction between moving parts [1]. Another type of wear is erosive wear due to impact of solid particles, which is known as solid particle erosion. Solid particle erosion (SPE) is a dynamic process of material removal from a target surface because of mechanical interaction between impinging particles and the target surface due to large-scale deformation, fracture, cutting, or a combination. Early studies of SPE were directed toward erosion prevention in pipelines and turbomachinery. Bitter studied SPE mechanisms [2,3], classifying them into brittle and cutting wear. In brittle SPE processes, deformation wear and fracture are the primary mechanisms, while in ductile SPE processes, cutting wear is the primary mechanism [2,4]. Since the early works of Bitter, the study of SPE has expanded from erosion prevention in pipelines to several industries, including aerospace, defense, renewable energy, biomedical sectors, and mining [5–9].

1.2. Process parameters affecting solid particle erosion

SPE is a complex process influenced by many parameters. Studies indicate that particle properties (size, density, sharpness, and hardness); impact parameters (angle, velocity, and impact duration); and target surface hardness influence the SPE rate (mass of material removed per mass of erodent used) [10–14]. Zambrano et al. investigated the complexity of wear regime predictions, correlating the abrasive fracture toughness, and the hardness ratio between the abrasive and the substrate [15]. Many researchers have reported that erosive wear rate depends on impact angle [7,8,13,[16–19]. During SPE, the incident particle's kinetic energy transferred to the target material depends on the mechanical properties of the target and the erodent. Many researchers [16,20–24] have focused on investigating the relationship between the bulk mechanical properties and the resulting SPE wear rate even though the thermal, mechanical, and chemical degradations

* Corresponding author.
E-mail addresses: wwcashmore@alaska.edu (W. Cashmore), ghailu@alaska.edu (G. Hailu).

https://doi.org/10.1016/j.triboint.2024.110439
Received 8 October 2024; Received in revised form 30 November 2024; Accepted 2 December 2024
Available online 10 December 2024

Nomenclature

A	Area of scar region ($pixels^2$)
D_n	Nozzle Diameter (mm)
D_p	Mean Particle Diameter (μm)
h	Distance between the nozzle tip and slotted disk (mm)
k	Coverage factor for uncertainty confidence interval conversion
l_e	Equivalent standoff distance from nozzle to measurement point (mm)
$\dot{m}$	Abrasive mass flow rate (g/min)
P	Driving pressure differential (kPa)
r	Radial distance from the shaft's axial centerline to the nozzle tip (mm)
s	Distance between the slotted disc and the recording disc (mm)
t	DDA test duration (s)
t_{rot}	The period of opportunity in which the slot opening is in alignment with the nozzle (s)
u_i	Measurement uncertainty of variable: i
V_{Cutoff}	Minimum particle velocity to pass through the slot without interaction with the slot-wall (m/s)
V_n	Traversal speed of the nozzle (Appendix A), (mm/s)
V_p	Mean abrasive particle velocity (m/s)
V_{wall}	Linear velocity of the inside face of the slot wall (m/s)
W_d	Width of the slotted disk (mm)
W_s	Width of the slot, on the slotted disk (mm)
x_c	X-axis location of scar centroid ($pixels$)
y_c	Y-axis location of scar centroid ($pixels$)
ϕ	Scar angle (°)
ε	Erosion efficiency
ρ	Particle density (g/cm^3)
σ_i	Standard deviation of variable i's measurements
ω	Disc angular velocity (RPM)

Nomenclature acronyms

DDA	Double disc anemometer
LDV	Laser Doppler velocimetry
PIV	Particle image velocimetry
PTV	Particle tracking velocimetry
RMS	Root mean square
SEM	Scanning electron microscope
SPE	Solid particle erosion

occurring during SPE can change the properties of the eroded layers from those of the bulk material [25]. Since mechanical properties change during SPE, other researchers have attempted to incorporate selected material properties (usually only one) and introduce empirical relationships to predict SPE wear [25–29]. For example, Sundararajan et al. [29] introduced a parameter known as erosion efficiency (ε), which they claim can identify the dominant micro-mechanism leading to SPE wear for a wide range of materials, including coatings, metals, and ceramics. Particle velocity is one of the most critical parameters influencing SPE. Solid particle erosive wear rate is usually assumed to be directly proportional to the power of the particle velocity [13,30–34]. Each method has its advantages depending on the specific requirements of the measurement, such as the speed of the particles, the medium in which they are moving, and the level of precision required. Particle velocity has been measured using various techniques. These include laser Doppler velocimetry (LDV), which measures velocity by analyzing the frequency shift of light scattered by moving particles [35–38]. Another method is particle image velocimetry (PIV), which includes measuring the displacement of particles during two laser flashes, whose time between pulses is known [39–41]. Particle Tracking Velocimetry (PTV) is another method to determine particle velocities, in which trajectories of individual particles in three-dimensional space are tracked [33,42,43]. At a fraction of the cost, an alternative approach to the abovementioned methods is velocity measurement with a double-disc anemometer (DDA). In this method, particle velocity is determined using the time it takes for particles to travel a known distance between two rotating discs mounted on the same shaft. Since 1975, the DDA has been used to measure solid particle velocities in gas-particulate flow streams [32]. The Double-Disc Method, developed by Ruff and Ives [32], uses two discs placed in a flow to measure particles' velocity based on the timing of their interaction with the discs. Several researchers have conducted experiments and numerical studies to verify and validate the accuracy of DDA velocity measurements and find correlative relationships applicable to determining particle velocities under broad experimental conditions [34]. Furthermore, the use of DDA has been extended to the measurement of particle velocity in abrasive slurry jets, and its accuracy has been improved by refining the design of the discs [44].

Previously documented by Gee and Hutchings [45] and tested and published by Stevenson and Hutchings [34], the accuracy of DDA measurements is published to be accurate to 5–10 % of the actual abrasive velocity. This error arises from systemic airflow influences, poor scarring, and inaccuracies in measuring scar centers. The airflow disturbances include aerodynamic influence from the spinning discs to the particulate stream [34,44,45]. Any induced out-of-plane particle motion will affect the mean velocity measurement.

While methods like particle imaging velocimetry (PIV), laser Doppler velocimetry (LDV), and laser shadowgraphy provide precise measurements, their implementation can be costly. This paper outlines the novel DDA design iteration and mean velocity measurement techniques used to improve SPE modelling using cost-effective equipment. Section 2 describes the novel design in detail, experimental setup, measurement procedures, and automated physics-based scar angle determination. The use of software assisted scar centroid analysis allows for unbiased consistency and new measurement uncertainty reporting procedures. Without previously being published, the measurement errors of a DDA are discussed and quantified. Post-processing for this experimental setup was completely automated, allowing for time-efficient data collection. Section 3 discusses the mean velocity measurement comparison between the DDA and the LDV, outlining the potential error sources and mitigation techniques. Additionally, in Appendix A, a novel study on slot geometries verifies design recommendations and clarifies the interaction between slot configurations and abrasive particles, enhancing the understanding of the resulting scarring.

2. Materials and experimental procedure

2.1. Double disc anemometer theory and componentry

Fundamentally, the DDA concept includes two discs mounted to a common rotating shaft (Fig. 1(a)). The abrasive particle blast is directed at the first slotted disc, periodically aligning and sending a slug of particle flow to interact with the recording disc after traveling across a known test section length, s. The angular difference between the slot and the recording disc's scarring determines the abrasive particles' mean linear velocity. During the period the particles travel linearly across the section length, s (Fig. 1(b)), a scarring angle, ϕ, develops between the slot entry and the resulting scar (Fig. 1(c)).

The mean linear velocity V_p, can be determined from the known scar angle ϕ, the length s, and the speed of the shaft ω. Eq. 1 gives the governing equation for the mean linear particle velocity calculation,

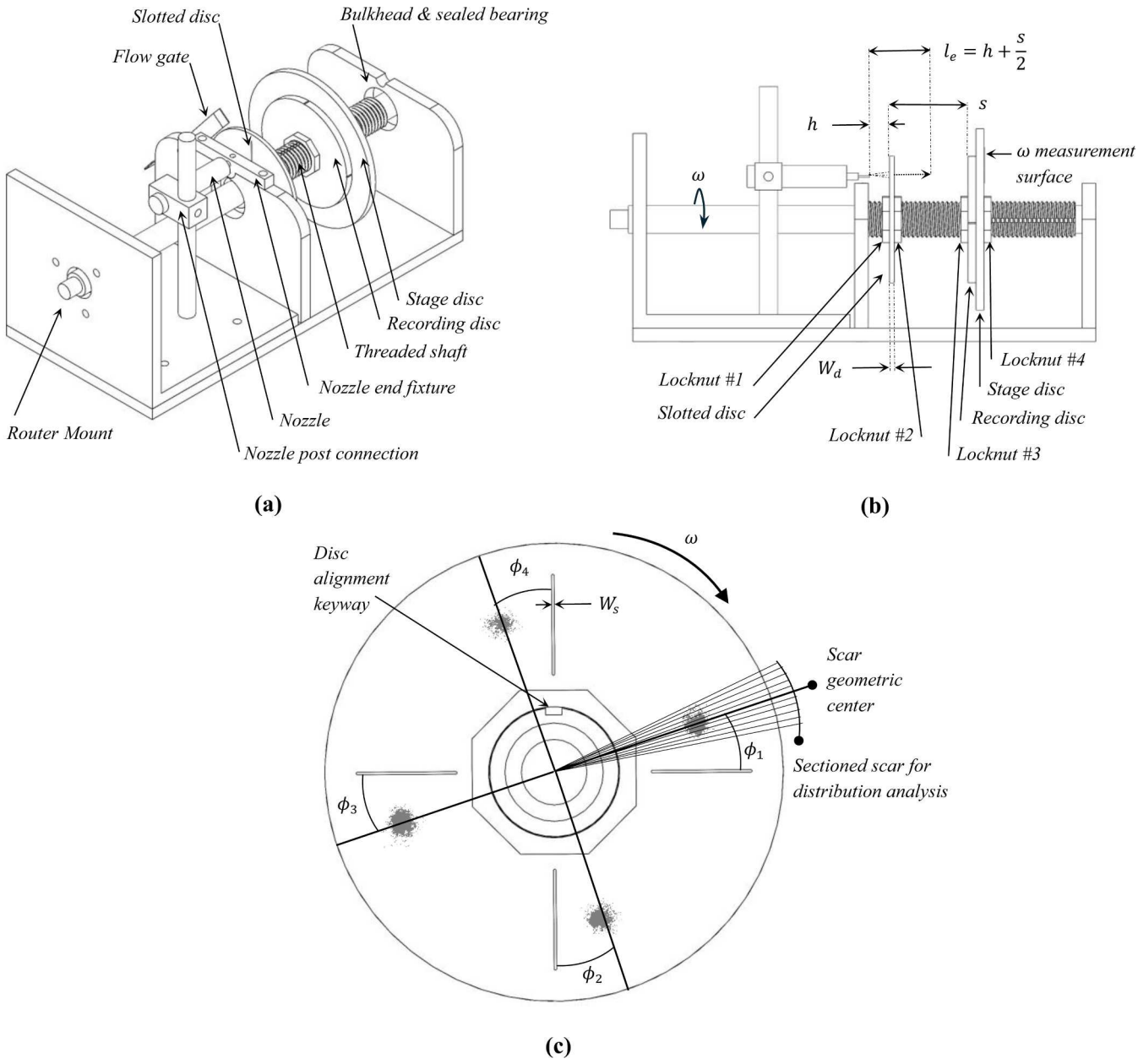

Fig. 1. (a) Labelled isometric view of the full assembly (b) Labelled DDA side-profile schematic (c) View of the overlapping slotted and recording discs.

accounting for unit conversion.

$$V_p = \frac{6 \bullet s \bullet \phi}{\omega} \tag{1}$$

Previous works well document the DDA's theoretical background. For an in-depth understanding of the underlying physics, refer to the work of Ruff and Ives [32] and Haghbin et al. [44].

Contrary to the DDA design of Haghbin et al. [44], a horizontal threaded shaft was adopted because it allowed for easy assembly and quick changing of parts. Mounted on the shaft are three discs: the slotted, recording, and staging disc (Fig. 1(b)), precisely aligned by engagement in a keyway. The slotted disc has four tapered slot openings, imparting four evenly distributed scars, on the recording disc for analysis. The stage disc is positioned directly behind the recording disc, providing stability and a consistent surface for angular velocity measurement, ω. A fixed base variable speed router powers the shaft rotation, the SKIL Model RT1323–00. All are mounted to a steel framework, rotating on sealed roller bearings. See (Fig. 1) for the labeled assembly and key variable definitions.

2.2. Double disc anemometer innovation

2.2.1. Horizontal adjustable test section

The threaded shaft allows for an adjustable test section and standoff distance adjustability. Discs are locked axially along the shaft using threaded locknuts. The discs and shaft are rotationally mated using a keyway to ensure slot alignment and perpendicularity. Testing can be time-consuming, so the DDA was designed to minimize the physical test setup. Only the end bulkhead and locknut #4 require unfastening to remove and replace the recording discs.

2.2.2. Tapered slots

It is vital to minimize the particle interaction with the slot wall. This interaction can include detrimental particle and wall collisions, nested slot air pocket effects, and rotary aerodynamic disturbances within the test section, s. Standard DDA fabrication has previously included a

square-cut slot [32,34,44,45], susceptible to interacting with abrasive particles. In the worst case, a range of slow particles may be given an insufficient time to travel through the slot (i.e., not all particles make it through), excluding these particles from the test data. To minimize particle and slot interaction, the shape of the slot can be fabricated to include an angled exit wall. As the abrasive particles enter the leading edge of the slot, the slot walls begin to recede (tapered slot), majorly eliminating particle and slot-wall collision. See Appendix A for the analysis of the slot geometries effect on the resulting scarring. To the best of the author's knowledge, testing, and analysis of slot geometry has not been previously published. In addition, this study introduces the particle velocity cutoff which characterizes the minimum particle velocity capable of passing through the slot. For an accurate mean velocity measurement, a DDA operator must attest that the full range of particle velocities are influencing the scar on the recording disc. The work in Appendix A challenges the previously used square-cut slot geometry to conclusively determine the tapered slotted disc as an improved slot geometry.

2.2.3. Nozzle perpendicular fixing

The governing equation assumes that the slotted and recording disks are parallel while the approaching abrasive particles travel along a normal trajectory. Mounting the nozzle on the DDA framework allows for consistent and precise alignment.

2.2.4. Flow gate

The addition of a gate to control the exposure allows for a fully developed particle flow from the beginning of the test. The developing flow phase of the utilized micro-blaster includes a purge on startup, which maintains the flow's consistency. The micro-blaster's purge should not be included in the erosive and velocity testing to maintain consistent results.

2.2.5. Recording disc imaging

Effectively capturing the scarring will require a well-lit photobooth. It is recommended to provide backlighting behind the acrylic recording disc; this will illuminate and sharply outline the edges and area of the scarring. An LED light panel is recommended to provide uniform illumination. The *Canon Inc*, *U.S.A.* EOS 80D camera and Macro EFS 35 mm lens were used to capture the recording disc photographs. See Fig. 2 for a labeled photobooth schematic.

2.2.6. Scar angle measurement automation

Previous publications have assessed the angle of the scar visually without determining a precise center [32,34,45]. This study utilizes physics-based image processing, which is superior due to its repeatability and accuracy, allowing for the removal of human judgment. A defined angle measurement procedure provides consistent and unbiased results post-processing. Furthermore, the use of image processing allows for quantifiable measurement uncertainty, which this study utilizes.

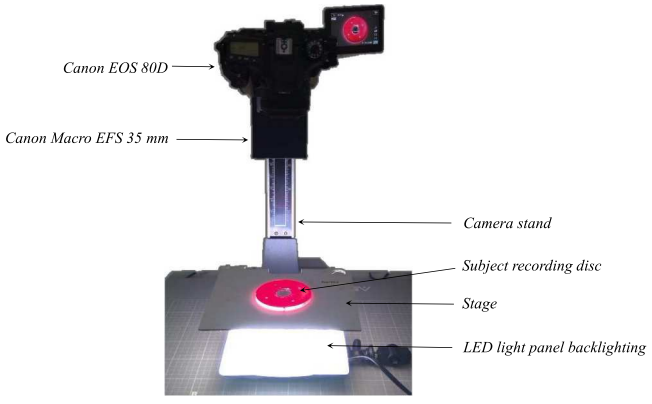

Fig. 2. Photobooth for recording disc imagery.

The scar angle measurement uncertainty was identified by fitting a normal (Gaussian) distribution to the scarred region's area and calculating the distribution fitting's confidence interval.

To precisely identify the mean scar angle, ϕ, the center of the scar region must be identifiable. The recording discs were cut from 5.5 mm thick uncoated clear acrylic. Acetone was used to clean the surface in preparation for painting. Scar testing was conducted for numerous types of paint, ideally identifying a paint that is removed with every particle impact without flaking. The best scarring was achieved using a water-based surveyor's temporary spray paint (*Rust-Oleum SKU:2564838*). The paint was sprayed from a distance of 1 m in a fine mist to achieve complete coverage of the thinnest possible coating. Essentially, the recording disc was primed to make all surface impact locations visible and detectable by photographic image analysis.

Haghbin et al.'s work [44] investigated the agreement of scar center locating, addressing the geometric mean, the location of the peak crater density, and the weighted average angle. The findings were published as fair agreement between the various scar angle measurement methods. In this work, the automated scar angle measurement (ϕ) was made using MATLAB® (Version 9.14 R2023a) and the 'Image Processing Toolbox (Version 11.7 R2023a).' Using the recording disc photography methods above (Section 2.2.5), images were taken ensuring the discs were correctly lit, centered, and parallel with the camera's lens. The recording disk was backlit to illuminate the paintless scarred region, with sufficient front lighting to distinguish the bright red paint sharply.

Using commercial software, MATLAB®, each recording disc image was converted to binary with a sensitivity threshold to distinguish the scarring. Each scar region was analyzed as a 2D shape, in which the centroid was identified as a weighted average of the area (Eqs. 2 and 3).

$$x_c = \frac{1}{A}\iint_A x dA \tag{2}$$

$$y_c = \frac{1}{A}\iint_A y dA \tag{3}$$

The angle was calculated from the center of the disc, between the tapered slot center and the geometric scar centroid. Interestingly, previous publications of the DDA discuss measuring the angle between a stationary scar ($\omega = 0\ RPM$) and the angularly displaced scar [34,45]. This process involves identifying two scar centers for a single-angle measurement, ϕ. Angle measurement can be made without the uncertainty of identifying the scar centroid twice. During post-processing, the center of the slot is identifiable by an indicator precisely cut on the recording disc.

2.3. Result validation equipment

Using Measurement Science Enterprise's miniLDV-G5–240 (*United States)*, particle velocity was recorded at incrementally increasing equivalent standoff distances, l_e. This distance is measured from the tip of the nozzle to the intersecting LDV laser. The LDV velocity data was compared to the DDA readings to compare a 'state-of-the-art' methodology to the DDA alternative measurements. Erosive testing conditions were maintained to ensure a valid comparison between velocity measurement instruments; see Table 1 for the erosive testing conditions. Comco Inc (*United* States) provided the abrasive particles and the pressurized blaster unit, 'Glass bead 50 μm' ejected from the AccuFlo micro-abrasive blaster at a controlled pressure of 160 kPa. Refer to Fig. 3, for a scanning electron microscope (SEM) image of the abrasive particles. The mass flow rate was measured using an abrasive collection container. The increase of the container's mass was reported over the blast period.

Table 1
Erosive testing conditions for all DDA and LDV tests.

Parameter	*Attributes*	*Measurement method / Supplier*
Erosive particles	Glass bead 50 μm	Comco Inc, United States.
Mean particle diameter, D_p	66.4 μm	MASTERSIZER 2000, Malvern Analytical Ltd, United Kingdom. D_p was determined as the volume weighted mean of the particle population.
Particle density, ρ	2.5 g/cm^3	Comco Inc datasheet PD1004_H
Particle shape	Spherical	Scanning electron microscope S-3400N S, Hitachi, Japan. Refer toFig. 3
Micro-abrasive blaster	AccuFlo	Comco Inc AccuFlo AF10 Standard Tank w/ Blast Timer
Nozzle diameter, D_n	0.76 mm	Comco Inc, P# MB2520 −30
Pressure, P	160 kPa	
Mass flow rate, $\dot{m}$	0.654 g/min	Measured a container's mass difference across a particle collection period.
Slot width, W_s	0.98 mm	Mitutoyo Digital Calipers. Average of 4 slots.

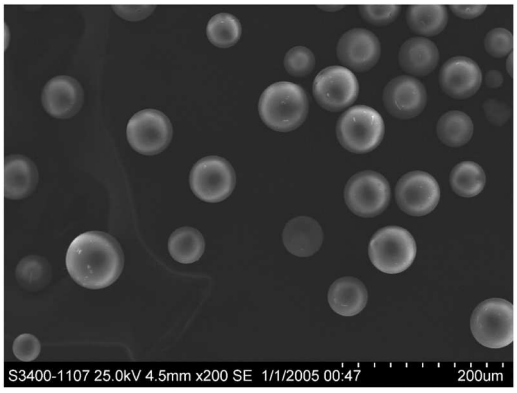

Fig. 3. Scanning electron microscope (SEM) image of abrasive particles.

2.4. Double disc anemometer procedure

2.4.1. Experiment testing conditions

The primary comparison made was the measured particle velocity by the DDA and the LDV at various equivalent standoff distances, l_e. Across the DDA test section, a position needed to be pin pointed to correspond to the measured particle velocity, as particle speeds are expected to decrease with distance from the nozzle. An assumption of constant change in particle velocity was made to approximate the standoff distance at the midpoint of the DDA's test section, s. For a DDA test, the equivalent standoff distance from the nozzle to the position of interest, l_e, was calculated as the sum of h and $s/2$ (Eq. 4). See Fig. 1(b).

$$l_e = h + \frac{s}{2} \tag{4}$$

2.4.2. Experiment procedure

User instructions on how to avoid common error sources during DDA operation are often missing in the literature. This section will outline the general recommended test procedure and some required practices for accurate particle velocity measurement using a DDA. To ensure clarity, the following steps detail the setup and measurement process, starting with the locknut and disc configuration along the threaded shaft.

Each locknut position sets each disc's position on the thread. The desired equivalent standoff distance to the accuracy of ±0.1 mm was difficult to pinpoint. However, the exact test section distance, s, could be measured precisely once assembled, using digital calipers (*Mitutoyo America Corporation, United States, P# 500–753-20*). The positioning of lock nut #1 (and #2) determines the flow development distance, h. Before inserting the recording disc, the desired separation distance, s, was set by adjusting lock nut #3. Then the recording disc and the stage disc was carefully inserted, protecting the visible faces. Scratches on the recording disc face will affect the result post-processing, while scratches on the matte stage disc face will affect the tachometer's measurement. Then the tachometer (*Nidec Corporation, Japan, DT-2100*) was positioned to acquire a non-contact angular velocity reading, toward the matte stage disc with a rotating reflective strip. Finally, all locknuts were tightened to limit failures, vibrations, and movement-inducing errors.

Rotational alignment between the slotted disc and the recording disc is required. The recording disc is fabricated with slot alignment notches, for pre-test checks and post-processing reference. Depending on the quality of fabrication tolerances, each disc's key fitment within the keyway may allow for misalignment. Alignment was checked by mounting a laser perpendicular to the assembly, ensuring the slots align with the reference notches [44].

For a valid measurement, all efforts need to be made to reduce macro and micro-roughness rotating at critical locations of the shaft. This roughness includes the circumferential notches of the locknuts and the surface of the thread. The aerodynamic influences on the air between the nozzle exit and the recording disc must be minimized to reduce unaccounted particle motion. Smooth shrink-wrap around the locknuts and the thread proved effective in testing to reduce the scarring scatter.

During exposure, ensure the flow is consistent with a stable particle feed and abrasive air mixture. The abrasive flow rate should be regulated using the flow gate, ensuring the micro-blaster flow is stable and steady before beginning the test.

The recording disc must be photographed correctly for accurate scar angle measurement. Essential elements of the capture include a stark contrast between the scarred and non-scarred regions and a centered view with the recording disc perpendicular to the view direction. Any unaccounted wide-angle lens distortion ('fisheye') or misalignment will cause angle measurement inaccuracies.

2.4.3. Computing the measurement uncertainty using Kline & McClintock method

The Kline & McClintock Method provides a detailed assessment of uncertainty by systematically evaluating the propagation of errors through the analysis, which often includes both random and systematic errors, providing a comprehensive view of the potential impact on the results. To implement the Kline & McClintock measurement uncertainty method [46], the type A (random) and type B (fixed) uncertainty were characterized. Type A uncertainty is the random error associated with repetitive measurement fluctuations. The total type A uncertainty, $u_{V_p type\ A}$, is calculated as the root mean square (RMS) of the measured variable's standard deviation and sensitivity effect, (Eq. 5). Each DDA trial provides multiple results as the slotted disc has four slots, resulting in four scar angle measurements. The type A uncertainty calculation considers the deviation of the spacing, σ_s, the deviation of the angular velocity, σ_ω, and the deviation of the measured mean scar angles, σ_ϕ.

$$u_{V_p typeA} = \sqrt{\left(\frac{dV_p}{ds} \bullet \sigma_s\right)^2 + \left(\frac{dV_p}{d\omega} \bullet \sigma_\omega\right)^2 + \left(\frac{dV_p}{d\phi} \bullet \sigma_\phi\right)^2} \tag{5}$$

Type B uncertainty is the systematic uncertainty of each measurement technique, outlined by the equipment's precision specifications. See Eq. 6 for how to calculate type B uncertainty. The reported total uncertainty is calculated as the RMS of the type A and type B uncertainties (Eq.7).

$$u_{V_p typeB} = \sqrt{\left(\frac{dV_p}{ds} \bullet \delta s\right)^2 + \left(\frac{dV_p}{d\omega} \bullet \delta\omega\right)^2 + \left(\frac{dV_p}{d\phi} \bullet \delta\phi\right)^2} \tag{6}$$

$$u_{V_p} = k \bullet \sqrt{\left(u_{V_p typeA}\right)^2 + \left(u_{V_p typeB}\right)^2} \tag{7}$$

Identifying the systematic uncertainty of the automated angle

measurement, $\delta\phi$, requires investigating the uncertainty of the normal distribution fitting. Each scar region is subdivided into 50 angular sections (See Fig. 1(c)). The area distribution between these segments can be analyzed to apply a normal distribution fit. There was excellent agreement between the measured scar centroid and the center of the fitted normal distribution. The systematic uncertainty of the automated angle measurement, $\delta\phi$, is the 67 % confidence interval of the normal distribution's fitted mean. Variables δs and $\delta\omega$, were outlined in the instrument specifications as the respective accuracy of the digital calipers and tachometer.

Discussed thoroughly throughout the works of Kline et al. [46] and Moffat [47], the uncertainty is reported as a confidence interval, within which the true mean is likely to be. The coverage factor, $k = 2$, is a conversion factor to report the normally distributed uncertainty from a 67 % to a 95 % confidence interval.

2.5. Optimized angular velocity

The angular velocity of the DDA, ω, should be a controlled variable with an insignificant effect on the measured result. The shaft rotation rate, in theory, should not affect the measured abrasive velocity. Section 3.3 outlines the results of incrementally increasing the angular velocity, reporting the resultant measured particle velocity, V_p, and the measurement uncertainty, u_{V_p}. All other testing conditions remain unchanged to gauge the effects of angular velocity independently.

3. Results and discussion

3.1. LDV results

LDV results illustrate predictable and expected particle velocity behavior. A developing phase is present, which the paper Li et al. discusses [48]. The abrasive particles accelerate to the pressurized air flow velocity before reaching a maximum. Beyond this point, the abrasive particles decelerate gradually [48]. Fig. 4 outlines the results of the flow characterization using the LDV unit, measuring the particle velocity distribution at incrementally increasing standoff distances from 5 mm to 50 mm.

The maximum particle velocity, $V_p = 95.3\ \frac{m}{s}$, occurs 14 mm from the nozzle tip, $l_e = 14mm$. The abrasive particle velocity has a normal distribution, verified by the incredible sampling rate of the LDV, capable of processing 100,000 unique velocity measurements per minute. See Fig. 4 plotting the window representing one standard deviation of velocity measurements, ◇: $V_p \pm 1\sigma$. The deviation of the particle velocity, σ_{V_p}, at a 50 mm standoff distance is 9.2 % greater than the standard deviation at a 5 mm standoff distance.

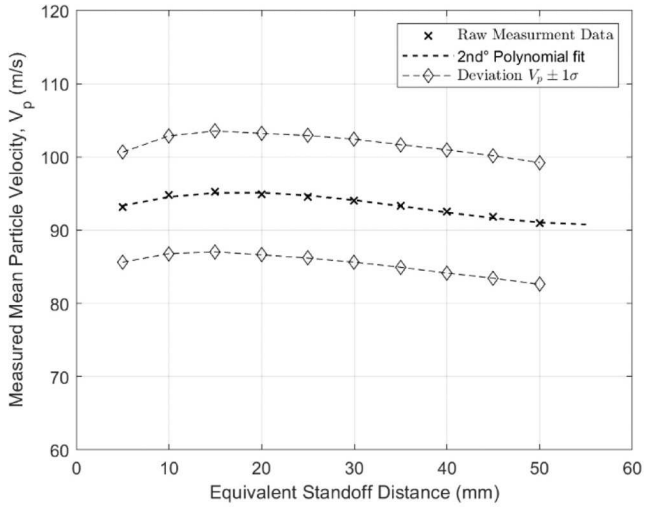

Fig. 4. Laser Doppler velocimetry flow characterization. See Table 2 for the controlled testing conditions.

3.2. Equivalent standoff distance comparison

This section interprets the comparison between two different measurement techniques: the highly accurate yet expensive LDV equipment and the comparatively inexpensive DDA. The comparison is conducted across controlled experimental conditions, see Table (2). The mean particle velocity is measured by the DDA and LDV at incrementally increasing standoff distances to good agreement.

Analyzing Fig. 5, the velocity, V_p, measured by the DDA is consistently under-reported. However, the mean error between the two methods is only -2.8 %. The maximum error differential between the test methods was -5.1 % and the minimum error differential was -0.04 %. All mean particle velocities measured by the DDA were firmly within the first standard deviation, σ, of the LDV measurements at all equivalent standoff distances tested. Although the DDA underreported the mean particle velocities, the LDV measurements were all within the calculated DDA uncertainty. The maximum uncertainty calculated was a significant $\pm 7.2\ m/s$ or ± 7.9 % at an equivalent standoff distance of $l_e = 14\ mm$. As the standoff distances increased, the reported uncertainty decreased, with a minimum calculated uncertainty of $\pm 3.0\ m/s$ or ± 3.2 % occurring at an equivalent standoff distance of $l_e = 25.4\ mm$. Given the undesirably large uncertainty of experimental tests of $l_e < 18\ mm$, the sensitivities of the uncertainty calculation were investigated. The mean velocity uncertainty calculation was highly sensitive to the angle measurement deviation across the four measured scars, σ_ϕ, which contributed to the majority of overall uncertainty (Eq. 5). The partial derivative, $\frac{dV_p}{d\phi}$, diminishes with an incrementally larger scar angle, ϕ, meaning the reported uncertainty is minimized with a large test section length, s. The data is inconclusive in attesting to higher accuracy measurements occurring at increasing standoff distances, as the results appear to be optimal from $l_e = 15\ mm$ to $17\ mm$. Refer to Appendix B for a sample DDA and LDV result report, including the overlayed scarring distribution fitments.

3.3. DDA angular velocity optimization

This section investigates the effect of angular velocities on mean particle velocity measurement and the corresponding uncertainty. When

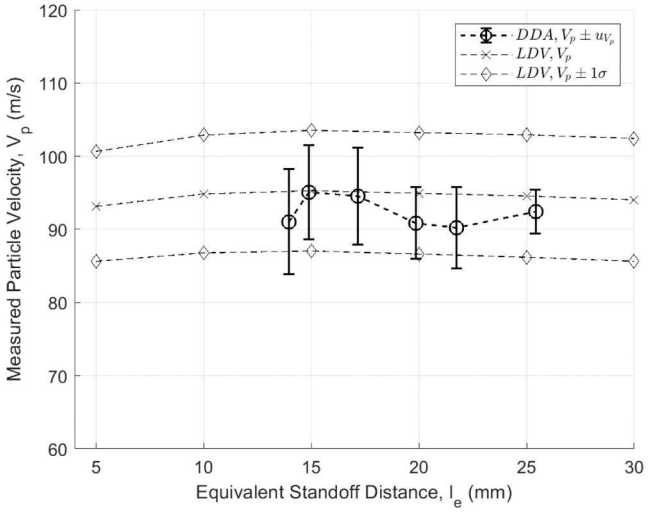

Fig. 5. DDA and LDV particle velocity measurement comparison at incrementally increased disc separation, s. $h = 5\ mm$, $\omega = 17{,}500$ RPM, $t = 60$ s. See Table 2 for the controlled testing conditions.

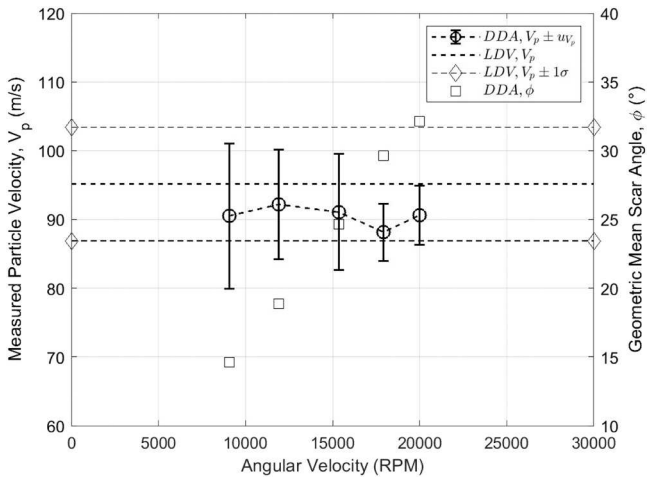

Fig. 6. A plot of angular velocities effect of DDA uncertainty and accuracy. h= 5 mm, s = 24 mm, t = 60 s, incrementally increased ω by 2750 RPM. See Table 2 for the controlled testing conditions.

measuring the particle velocity for a set of given experimental conditions, there is a free choice of the power unit's angular velocity, ω. This controlled variable, ω, will directly affect the resulting scar angle, ϕ, and in theory should not directly affect the measured particle velocity, V_p. The shape and quality of the scarring depends upon the angular velocity, ω. Referring to the right axis of Fig. 6, with an incremental increase of ω the scarring angle ϕ increases linearly, in agreement with the expected behavior of the governing equation (Eq.1).

The test results (Fig. 6) are inconclusive of an optimal operation setting for the controlled testing conditions. The maximum uncertainty occurs at the lowest angular velocity setting of $\omega = 9,000\,RPM$, reporting $u_{V_p} = \pm 10.6\,m/s$ or ± 11.7 %. The minimum uncertainty occurs at the highest angular velocity setting of $\omega = 20,000\,RPM$, reporting $u_{V_p} = \pm 4.3\,m/s$ or ± 4.7 %. Similar to the trends of the Section 3.2 results, the partial derivative $\frac{dV_p}{d\phi}$ is minimized with a large angle measurement ($\phi > 30°$), significantly decreasing the reported mean velocity uncertainty. This theoretical reasoning suggests that the DDA should be operated at the greatest possible angular velocity to increase the scar angle, ϕ, and consequently minimize the uncertainty. Despite the more desirable uncertainty reporting, there does not appear to be a correlation between the angular velocity and result accuracy within the limited testing data. The plotted errors appear to be scattered, with a maximum error of -7.4 % occurring at $\omega = 18000\,RPM$, and a minimum error of -3.1 % occurring at $\omega = 12000\,RPM$. Without further testing and indicative data, the protocol for angular velocity selection should satisfy a criterion; this includes sufficient scarring angle for reliable measurement ($\phi > 20°$) and a reasonable reporting uncertainty ($u_{V_p} < \pm 5$ %).

4. Conclusions

- The double disc anemometer (DDA) requires careful operative procedures to produce reliable results. The DDA does not provide the accuracy available of alternative velocimetry methods, such as LDV equipment. The experimental testing of 66 μm glass bead abrasive blasted with a maximum mean particle velocity of 95.3 m/s, indicates the DDA is a fine alternative that reliably produces measurements within ± 5.1 % of the true mean particle velocity with a mean error of -2.8 %.
- Implementing an automated scar angle measurement allows for repeatable and unbiased results with quantifiable uncertainty. All mean velocity measurements made in Section 3.2 using the LDV were with the DDA's 95 % confidence interval uncertainty, with an optimal reported uncertainty of ± 3.2 %.
- The calculation of uncertainty is highly sensitive to deviations in angle measurements across the four observed scars. This uncertainty decreases as the scar angles increase, which is controlled by shaft angular velocity and standoff distances. For accurate mean velocity measurements, it is recommended that the scar angle, $\phi > 20°$, and a reporting uncertainty, $u_{V_p} < \pm 5$ %.
- To conduct accurate DDA measurements the scarring region must be minimally misaligned and distorted. Importantly, a tapered slotted disc is experimentally proven to provide enhanced results (Appendix A).

Statement of originality

We hereby declare that this original work has not been published previously and is not under consideration for publication in another journal. The authors have no other relevant affiliations or financial conflict with the subject maters or materials discussed in the manuscript. We further confirm that all authors have checked the manuscript and have agreed to the submission.

CRediT authorship contribution statement

William Cashmore: Writing – original draft, Software, Investigation, Formal analysis. **Alexander Blanchard:** Writing – review & editing, Resources, Methodology. **Getu Hailu:** Writing – review & editing, Supervision, Project administration, Methodology, Investigation, Funding acquisition, Conceptualization.

Declaration of Competing Interest

The authors declare the following financial interests/personal relationships which may be considered as potential competing interests: Dr. Getu Hailu reports financial support was provided by NSF, NASA. If there are other authors, they declare that they have no known competing financial interests or personal relationships that could have appeared to influence the work reported in this paper.

Acknowledgements

This research was supported by NSF Grant 2327252 and NASA Grant Number 80NSSC24K0486. The authors acknowledge the contribution of the senior capstone team, Jacob Bodolosky, Aaron Edora, Garrett Hassell, and Max Osborne, who developed and fabricated the initial DDA design.

Appendix A. Analysis of slot shape and particle interaction

As mentioned in Section 2.2.2, minimizing the interaction between the slot wall and the abrasive particles is essential for a valid velocity measurement. Particles must have sufficient opportunity to travel through the slot without colliding with the rotating inside wall of the slot. Analyzing the interaction of particles colliding with a square slot wall can be done by considering the slot and nozzle alignment period. The slot's alignment period with the nozzle must exceed the period for abrasive particles to travel through the width of the disc. The slowest particle capable of passing through the square-slot without collision can be calculated, referred to as the 'velocity cutoff,' V_{cutoff}. Purely considering the kinematics and omitting the airflow effects, the test parameters that influence the velocity cutoff are angular velocity (ω), slot width (W_s), disc width (W_d), and radial distance (r).

See Table A.1 for the V_{cutoff} equation derivation. Refer to Figure A.1 for parameter definitions.

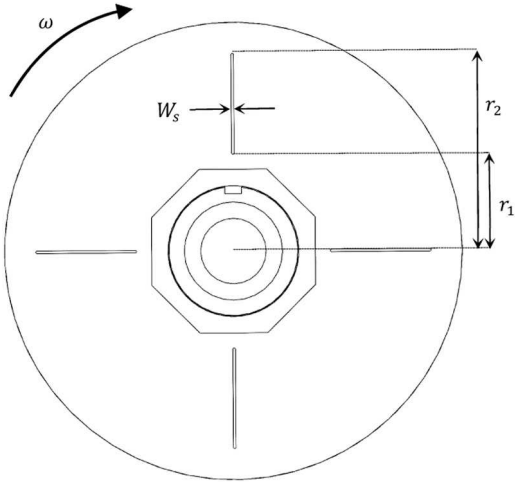

Fig. A.1. Schematic of the slotted disc outlining the key parameters to calculate the velocity cutoff.

Table A.1
Derivation of the velocity cutoff.

Equation	*Eqn. #*	*Explanation.*
$V_{wall} = r\omega$	Eqn. A.1	The linear velocity of the slot wall (V_{wall}), travelling perpendicular to the abrasive particle.
$t_{rot} = \frac{W_s}{V_{wall}}$	Eqn. A.2	The period of opportunity (t_{rot}), which the slot opening is in alignment with the nozzle.
$V_{cutoff} = \frac{W_d}{t_{rot}}$	Eqn. A.3	The minimum particle speed to pass through the slot when entering at the optimal position.
$V_{cutoff} = \frac{W_d r\omega}{W_s}$	Eqn. A.4	Collating equations A.1 - A.3. (Standard S.I base units).
$V_{cutoff} = \frac{\pi\, W_d r\omega}{30000 W_s}$	Eqn. A.5	Velocity cutoff equation, accounting for unit conversion. ($\omega : RPM,\ W_d : mm,\ W_S : mm, r : mm$)

A test was implemented to verify the slot-wall and particle interaction hypothesis for the square-cut slot. The test intended to challenge the velocity cutoff for the square-cut slot and compare the scarring results with the improved tapered slot design. By implementing a traversing nozzle, the radial distance from the centroid (r) was variably oscillated between the bottom and the top of the slot (r_1 and r_2). Consequently, the velocity cutoff (V_{cutoff}) was expected to increase linearly with an increasing radial distance from the shaft center. See Table A.2 for the implemented testing conditions and see Table A.3 for the calculated velocity cutoff at each radial position (using Eqn. A.5).

Table A.2
Traversal nozzle erosion testing parameters.

Parameter	*Attributes*	*Measurement method / Supplier*
Radial distance from bottom of the slot, r_1	19.1 *mm*	Mitutoyo Digital Calipers. Average of 4 slots.
Radial distance from top of the slot, r_2	44.5 *mm*	Mitutoyo Digital Calipers. Average of 4 slots.
Angular velocity, ω	14100 *RPM*	Nidec, DT−2100 Tachometer.
Slot width, W_s	0.98 *mm*	Mitutoyo Digital Calipers. Average of 4 slots.
Slotted disc thickness, W_d	3.1 *mm*	Mitutoyo Digital Calipers. Average thickness at each slot.
Nozzle traversal speed, V_n	1.4 mm/s	Step motor driven two-axis stage, with attached nozzle post.
Mean particle velocity, V_p	94.5 m/s	Expected particle velocity, given the characterization of Section 3.1 *LDV Results.*

See Figure A.2 for the scarring results from the traversal nozzle tests for both the square-cut slotted disc and the tapered slotted disc exposed to the controlled erosion conditions (See Table 2). The tapered slotted disc developed scarring, which was well-grouped, radially consistent, and angularly uniform (Figure A.2(a)). When using the tapered slot geometry, the radial positioning (r) has no apparent scarring influence as the scarring angle (ϕ) is consistent from r_1 to r_2. Visible in Figure A.2(b) is the scarring results from the square-cut slot geometry. The scarring is indicative of significant interaction between the abrasive particles and the square-cut slot wall. The scarring lands in two distinguished regions, the 'expected region' and the 'interaction region' (Fig. A.3). The square-cut slot did produce scarring at the expected scarring angle (ϕ), however, this scarring only developed radially from $r_1 = 19.1\ mm$ to $r = 30.5\ mm$ (Fig. A.3). Particles which collided with the slot wall, landed in the interaction region. This scarring does not correlate to appropriate velocity measurement, mostly aligning and exceeding the slot's position ($\phi = 0°\ or\ \phi < 0°$).

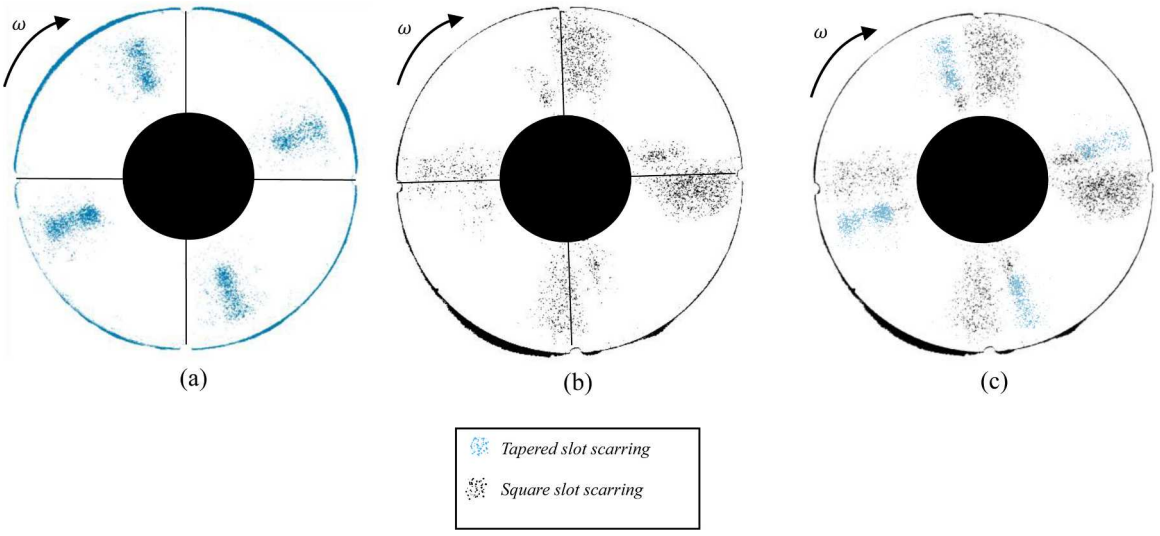

Fig. A.2. Resultant scarring from the traversal nozzle testing. See Table A.2 for the test parameters. (a) Tapered slots, (b) Square-cut slots, (c) Overlay of the resultant scarring from both slot geometries.

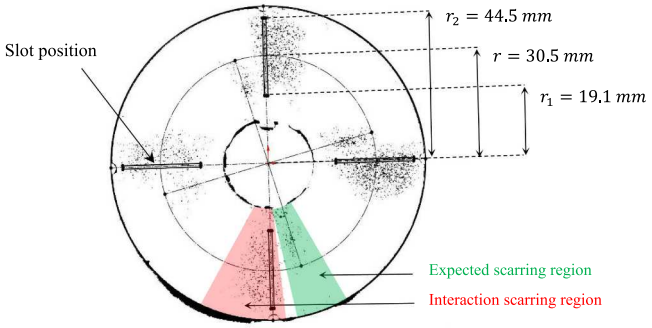

Fig. A.3. Resultant scarring of the square-cut slot, with a scribe of the scarring's largest radial position.

.

Applying the velocity cutoff equation (Eqn. A.5) the square-slot's radially discontinuous scarring is understandable. See Table A.3. At the bottom of the slot (r_1) scarring is expected; the velocity cutoff calculated is $V_{cutoff} = 89.0\ m/s$, less than the expected particle velocity $V_p = 94.5\ m/s$. Whereas, at the top of the square-cut slot (r_2), $V_{cutoff} = 207.6\ m/s$, significantly exceeding the expected particle velocity. Simply, the abrasive particles are not allowed to travel through the slot, particles are colliding with the slot wall forming scarring in the interaction scarring region. The expected scarring furthest from the shaft's centerline, occurs at $r = 30.5\ mm$, corresponding to $V_{cutoff} = 142.5\ m/s$. This velocity cutoff reading is more than five standard deviations larger than the mean abrasive velocity, indicating that the square-cut slot's unaccounted aerodynamic effects influence the particles' travel. The traversal nozzle test results indicate that the square-cut slot may induce many detrimental particle influences when there is insufficient opportunity for particles to pass through the opening. The tapered slotted disc accommodated the intended scarring and particle trajectory, for a more reliable velocity measurement.

Table A.3
Calculation of the velocity cutoff at position r_1 and r_2, using Eqn. A.4 and Table A.2.

Radial Location	*Corresponding velocity cutoff*
Bottom of the slot: $r_1 = 19.1\ mm$	$V_{cutoff} = 89.0\ m/s$
Top of the slot: $r_2 = 44.5\ mm$	$V_{cutoff} = 207.6\ m/s$
Radial top of the square slot scarring: $r = 30.5\ mm$	$V_{cutoff} = 142.5\ m/s$

Appendix B. Data – Sample DDA test report & LDV plot

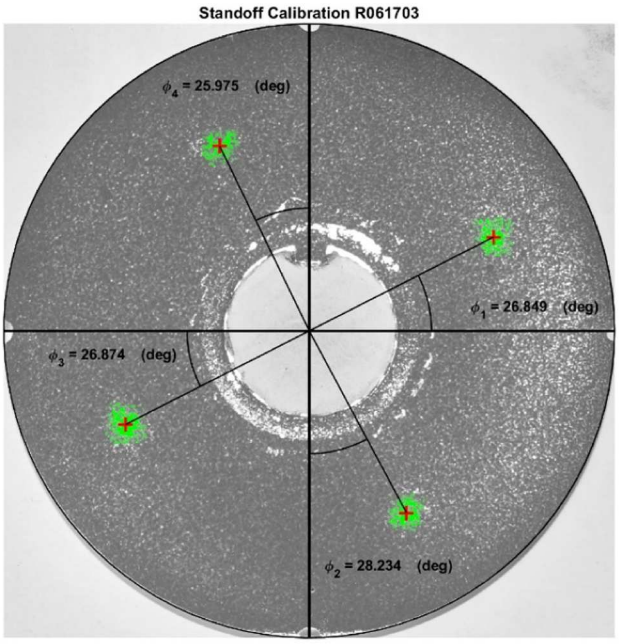

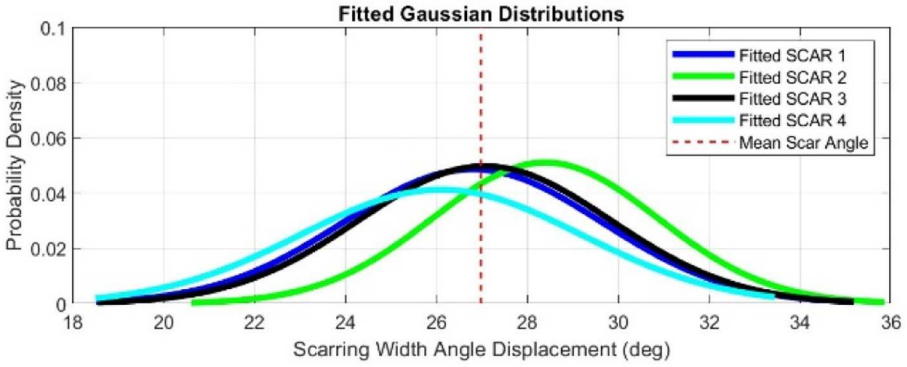

DDA TEST INFORMATION

OPERATOR:	William Cashmore					
DATE:	06/17/2024					
PARTICLE:	GlassBeads 50um		MEAN SCAR ANGLE:		26.983	deg
EXPOSURE:	60s		SCAR UNCERTIANTY:	+/-	0.116	deg
S (mm):	24.345					
RPM:	17462.6					
MEAN PARTICLE Dp:	66.5	μm	**MEAN VELOCITY:**		**94.5332**	**m/s**
DENSITY ρ:	2.5	g/cm3	UNCERTAINTY:	+/-	6.603	m/s
PRESSURE P:	160	kPa	UNCERTAINTY:	+/-	6.985	%
NOZZLE EXIT Dn:	0.76	mm				
SLOT: 0.75mm			**Equivalent Standoff:**		**17.1725**	**mm**
h: 5mm						

Fig. B.1. Sample collated results from DDA test, $l_e = 17.17\ mm$. See Section 3.2.

.

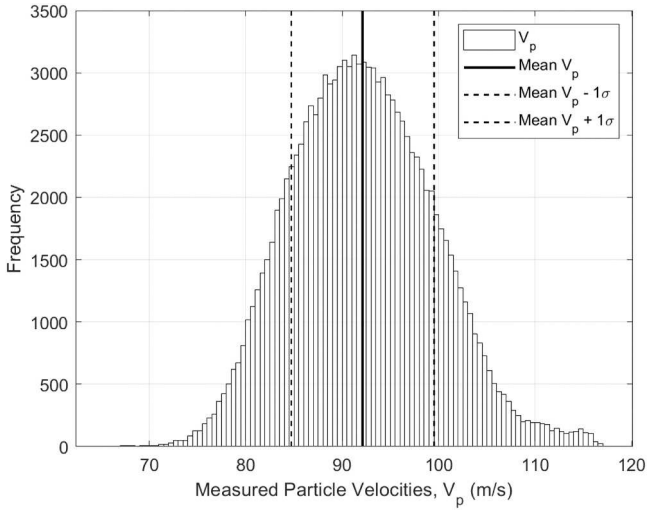

Fig. B.2. *Histogram plot of a LDV measurement.* $l_e = 20$ *mm,* $\mu = 92.13$ *m/s,* $\sigma = 7.40$ *m/s. See* Table 2 *for the controlled erosion conditions.*

.

Appendix C. Data Accessibility – Shared Data Repository

The following data repository provides public availability to the experimental processing script, written to automate the scar analysis and uncertainty calculations as discussed in Sections '*2.2.5. Scar angle measurement automation*' and '2.4.3. *Computing the measurement uncertainty using Kline & McClintock method.*' If any of the resources in this dataset are used in support of future published work, please credit the authors of the primary manuscript publication.

The following is available:

- The MATLAB® post-processing script, which is set to run an example DDA processing calculation from this experiment.
- The captured image of a recording disc, which is required to process the provided example DDA calculation.
- The abrasive flow velocity characterization made by the LDV equipment.

Cashmore, William; Blanchard, Alexander; Hailu, Getu (2024), "Accurate Measurement of Particle Velocity using a Double Disc Anemometer in Erosive Wear Experiments - Data", Mendeley Data, V1, doi: 10.17632/54xtyt2nfz.1.

Data availability

Data will be made available on request.

References

[1] Chen D, Rui, Zhao Bin, Xin Qi, Niu Xiaoxiao, Xie Zhongliang, et al. Analysis of transient lubrication and wear coupling behaviors considering thermal effect and journal misalignment for main bearings under dynamic load. Wear 2024;554–555:205478.
[2] Bitter JGA. A study of erosion phenomena Part I. Wear 1963. doi: 10.1016/0043-1648(63)90003-6.
[3] Bitter JGA. A study of erosion phenomena. Part II. Wear 1963. https://doi.org/10.1016/0043-1648(63)90073-5.
[4] Arrington S. Pipeline debris removal requires extensive planning. Pipeline Gas J 2006.
[5] Zhang S, Zhang J, Zhu B, Niu S, Han Z, Ren L. Progress in bio-inspired anti-solid particle erosion materials: learning from nature but going beyond nature. Chin J Mech Eng (Engl Ed) 2020. https://doi.org/10.1186/s10033-020-00458-y.
[6] Alqallaf J, Ali N, Teixeira JA, Addali A. Solid particle erosion behaviour and protective coatings for gas turbine compressor blades-a review. Processes 2020. https://doi.org/10.3390/PR8080984.
[7] Miyazaki N. Solid particle erosion of composite materials: a critical review. J Compos Mater 2016. https://doi.org/10.1177/0021998315617818.
[8] Galiullin T, et al. High temperature oxidation and erosion of candidate materials for particle receivers of concentrated solar power tower systems. Sol Energy 2019. https://doi.org/10.1016/j.solener.2019.06.057.
[9] Atapek ŞH, Fidan S. Solid-particle erosion behavior of cast alloys used in the mining industry. Int J Miner Metall Mater 2015. https://doi.org/10.1007/s12613-015-1196-6.
[10] Finnie I. Erosion of surfaces by solid particles. Wear 1960. https://doi.org/10.1016/0043-1648(60)90055-7.
[11] Tilly GP. Sand erosion of metals and plastics: a brief review. Wear 1969. https://doi.org/10.1016/0043-1648(69)90048-9.
[12] Winter RE, Hutchings IM. Solid particle erosion studies using single angular particles. Wear 1974. https://doi.org/10.1016/0043-1648(74)90069-6.
[13] Slikkerveer PJ, Veld FHIT. Model for patterned erosion 1999. https://doi.org/10.1016/S0043-1648(99)00177-5.
[14] Barkoula NM, Karger-Kocsis J. Processes and influencing parameters of the solid particle erosion of polymers and their composites. J Mater Sci 2002. https://doi.org/10.1023/A:1019633515481.
[15] Zambrano OA, García DS, Rodríguez SA, Coronado JJ. The mild-severe wear transition in erosion wear. Tribol Lett 2018. https://doi.org/10.1007/s11249-018-1046-6.
[16] The. erosion and deformation of polyethylene by solid-particle impact. Philos Trans R Soc Lond Ser A Math Phys Sci 1987. https://doi.org/10.1098/rsta.1987.0016.
[17] Oka YI, Ohnogi H, Hosokawa T, Matsumura M. The impact angle dependence of erosion damage caused by solid particle impact. Wear 1997. https://doi.org/10.1016/S0043-1648(96)07430-3.
[18] Finnie I, Stevick GR, Ridgely JR. The influence of impingement angle on the erosion of ductile metals by angular abrasive particles. Wear 1992. https://doi.org/10.1016/0043-1648(92)90206-N.
[19] Tewari US, Harsha AP, Häger AM, Friedrich K. Solid particle erosion of carbon fibre- and glass fibre-epoxy composites. Compos Sci Technol 2003. https://doi.org/10.1016/S0266-3538(02)00210-5.
[20] Brandstädter A, Goretta KC, Routbort JL, Groppi DP, Karasek KR. Solid-particle erosion of bismaleimide polymers. Wear 1991. https://doi.org/10.1016/0043-1648(91)90126-F.
[21] Trezona RI, Pickles MJ, Hutchings IM. Full factorial investigation of the erosion durability of automotive clearcoats. Tribol Int 2000. https://doi.org/10.1016/S0301-679X(00)00106-7.

[22] Rao PV, Young SG, Buckley DH. Solid spherical glass particle impingement studies of plastic materials. NASA Tech Pap 1983.
[23] Oka YI, Matsumura M, Kawabata T. Relationship between surface hardness and erosion damage caused by solid particle impact. Wear 1993. https://doi.org/10.1016/0043-1648(93)90067-V.
[24] Slikkerveer PJ, Touwslager FJ. Erosion of elastomeric protective coatings. Wear 1999. https://doi.org/10.1016/S0043-1648(99)00268-9.
[25] Li J, Hutchings IM. Resistance of cast polyurethane elastomers to solid particle erosion. Wear 1990. https://doi.org/10.1016/0043-1648(90)90032-6.
[26] Hutchings IM, Deuchar DWT, Muhr AH. Erosion of unfilled elastomers by solid particle impact. J Mater Sci 1987. https://doi.org/10.1007/BF01133360.
[27] Lancaster JK. Material-specific wear mechanisms: relevance to wear modelling. Wear 1990. https://doi.org/10.1016/0043-1648(90)90200-T.
[28] Oka YI, Yoshida T. Practical estimation of erosion damage caused by solid particle impact: Part 2: Mechanical properties of materials directly associated with erosion damage 2005. https://doi.org/10.1016/j.wear.2005.01.040.
[29] Sundararajan G, Roy M, Venkataraman B. Erosion efficiency-a new parameter to characterize the dominant erosion micromechanism. Wear 1990. https://doi.org/10.1016/0043-1648(90)90096-S.
[30] Pool KV, Dharan CKH, Finnie I. Erosive wear of composite materials. Wear 1986. https://doi.org/10.1016/0043-1648(86)90043-8.
[31] Roy M, Vishwanathan B, Sundararajan G. The solid particle erosion of polymer matrix composites. Wear 1994. https://doi.org/10.1016/0043-1648(94)90358-1.
[32] Ruff AW, Ives LK. Measurement of solid particle velocity in erosive wear. Wear 1975. https://doi.org/10.1016/0043-1648(75)90154-4.
[33] Mansouri A, Khanouki HA, Shirazi SA, McLaury BS. Particle tracking velocimetry (PTV) measurement of abrasive microparticle impact speed and angle in both air-sand and slurry erosion testers 2016. https://doi.org/10.1115/FEDSM2016-7768.
[34] Stevenson ANJ, Hutchings IM. Scaling laws for particle velocity in the gas-blast erosion test. Wear 1995. https://doi.org/10.1016/0043-1648(95)90008-X.
[35] Li Y, Li T, Zhang H, Sun Q, Ying W. LDV measurements of particle velocity distribution and annular film thickness in a turbulent fluidized bed. Powder Technol 2017. https://doi.org/10.1016/j.powtec.2016.10.028.
[36] Miska S, Shirazi SA, McLaury BS, Zhang Y, Rybicki EF, Okita R. Particle, fluid velocity, and erosion measurements for viscous liquids in a submerged direct impingement flow 2010. https://doi.org/10.1115/FEDSM-ICNMM2010-31269.
[37] Kliafas Y, Holt M. LDV measurements of a turbulent air-solid two-phase flow in a 90° bend. Exp Fluids 1987. https://doi.org/10.1007/BF00776177.
[38] Okita R, Zhang Y, McLaury BS, Shirazi SA, Rybicki EF. Effects of viscosity, particle size, and particle shape on erosion in gas and liquid flows 2011. https://doi.org/10.1115/AJK2011-09023.
[39] Scharnowski S, Kähler CJ. Particle image velocimetry - classical operating rules from today's perspective. Opt Lasers Eng 2020. https://doi.org/10.1016/j.optlaseng.2020.106185.
[40] Rajkumar YR, Shirazi SA, Karimi S. Particle size and concentration effects on solid particle erosion with PIV measurements of particle velocities 2020. https://doi.org/10.1115/FEDSM2020-20080.
[41] Li G, Li Z, Gao Z, Wang J, Bao Y, Derksen JJ. Particle image velocimetry experiments and direct numerical simulations of solids suspension in transitional stirred tank flow. Chem Eng Sci 2018. https://doi.org/10.1016/j.ces.2018.06.073.
[42] Lin N, He R, Zhang H, Wang J, Ma H, Huang H. Effect of particle flow rates on erosion ratio in particle impingement experiments 2020. doi: 10.1088/1757-899X/746/1/012013.
[43] Gietzen E, Karimi S, Goel N, Shirazi SA, Keller M, Otanicar T. Experimental investigation of low velocity and high temperature solid particle impact erosion wear. Wear 2022. https://doi.org/10.1016/j.wear.2022.204441.
[44] Haghbin N, Khakpour A, Schwartzentruber J, Papini M. Measurement of abrasive particle velocity and size distribution in high pressure abrasive slurry and water micro-jets using a modified dual disc anemometer. J Mater Process Technol 2019. https://doi.org/10.1016/j.jmatprotec.2018.08.014.
[45] Gee M, Hutchings I. General approaches and procedures for erosive wear testing: good practice guide 056 2002. Available: http://publications.eng.cam.ac.uk/328090/.
[46] Kline SJ, McClintock FA. Describing uncertainty in single sample experiments. Mech Eng 1953. Available: https://ci.nii.ac.jp/naid/10007206317/.
[47] Moffat RJ. Describing the uncertainties in experimental results. Exp Therm Fluid Sci 1988. https://doi.org/10.1016/0894-1777(88)90043-x.
[48] Li HZ, Wang J, Fan JM. Analysis and modelling of particle velocities in micro-abrasive air jet. Int J Mach Tools Manuf 2009. https://doi.org/10.1016/j.ijmachtools.2009.05.012.